Synchronized renal tubular cell death involves ferroptosis

Andreas Linkermann[a,1], Rachid Skouta[b], Nina Himmerkus[c], Shrikant R. Mulay[d], Christin Dewitz[a], Federica De Zen[a], Agnes Prokai[e], Gabriele Zuchtriegel[f,g], Fritz Krombach[f,g], Patrick-Simon Welz[h,i], Ricardo Weinlich[j], Tom Vanden Berghe[k,l], Peter Vandenabeele[k,l], Manolis Pasparakis[i], Markus Bleich[c], Joel M. Weinberg[m], Christoph A. Reichel[f,g], Jan Hinrich Bräsen[n], Ulrich Kunzendorf[a], Hans-Joachim Anders[d], Brent R. Stockwell[o,p,q,r], Douglas R. Green[j], and Stefan Krautwald[a,1]

[a]Clinic for Nephrology and Hypertension, Christian-Albrechts-University Kiel, 24105 Kiel, Germany; [b]Department of Biological Sciences and Department of Chemistry, University of Texas at El Paso, El Paso, TX 79902; [c]Department of Physiology, Christian-Albrechts-University Kiel, 24098 Kiel, Germany; [d]Nephrologisches Zentrum, Medizinische Klinik und Poliklinik IV, Klinikum der Universität München, Ludwig-Maximilians-Universität München, 80366 Munich, Germany; [e]First Department of Pediatrics, Semmelweis University, H-1083 Budapest, Hungary; [f]Department of Otorhinolaryngology, Head and Neck Surgery, Ludwig-Maximilians-Universität München, 81366 Munich, Germany; [g]Walter Brendel Centre of Experimental Medicine, Ludwig-Maximilians-Universität München, 81366 Munich, Germany; [h]Institute for Research in Biomedicine, 08028 Barcelona, Spain; [i]Institute for Genetics, University of Cologne, 50931 Cologne, Germany; [j]Department of Immunology, St. Jude Children's Research Hospital, Memphis, TN 38105-3678; [k]Molecular Signaling and Cell Death Unit, Inflammation Research Center, Vlaams Instituut voor Biotechnologie, Ghent University, 9052 Ghent, Belgium; [l]Methusalem Program, Ghent University, 9052 Ghent, Belgium; [m]Division of Nephrology, Department of Internal Medicine, VA Healthcare System and University of Michigan, Ann Arbor, MI 48109-5676; [n]Department of Pathology, University of Hannover, 30625 Hannover, Germany; [o]Department of Biological Sciences, Columbia University, New York, NY 10027; [p]Department of Chemistry, Columbia University, New York, NY 10027; [q]Howard Hughes Medical Institute, Columbia University, New York, NY 10027; and [r]Department of Systems Biology, Columbia University Medical Center, New York, NY 10027

Edited* by Vishva M. Dixit, Genentech, San Francisco, CA, and approved October 10, 2014 (received for review August 12, 2014)

Receptor-interacting protein kinase 3 (RIPK3)-mediated necroptosis is thought to be the pathophysiologically predominant pathway that leads to regulated necrosis of parenchymal cells in ischemia–reperfusion injury (IRI), and loss of either Fas-associated protein with death domain (FADD) or caspase-8 is known to sensitize tissues to undergo spontaneous necroptosis. Here, we demonstrate that renal tubules do not undergo sensitization to necroptosis upon genetic ablation of either FADD or caspase-8 and that the RIPK1 inhibitor necrostatin-1 (Nec-1) does not protect freshly isolated tubules from hypoxic injury. In contrast, iron-dependent ferroptosis directly causes synchronized necrosis of renal tubules, as demonstrated by intravital microscopy in models of IRI and oxalate crystal-induced acute kidney injury. To suppress ferroptosis in vivo, we generated a novel third-generation ferrostatin (termed 16-86), which we demonstrate to be more stable, to metabolism and plasma, and more potent, compared with the first-in-class compound ferrostatin-1 (Fer-1). Even in conditions with extraordinarily severe IRI, 16-86 exerts strong protection to an extent which has not previously allowed survival in any murine setting. In addition, 16-86 further potentiates the strong protective effect on IRI mediated by combination therapy with necrostatins and compounds that inhibit mitochondrial permeability transition. Renal tubules thus represent a tissue that is not sensitized to necroptosis by loss of FADD or caspase-8. Finally, ferroptosis mediates postischemic and toxic renal necrosis, which may be therapeutically targeted by ferrostatins and by combination therapy.

regulated cell death | programmed cell death | ferroptosis | necroptosis | apoptosis

Regulated cell death may result from immunologically silent apoptosis or from immunogenic necrosis (1–3). Necroptosis, the best-characterized pathway of regulated necrosis, involves activation of receptor-interacting protein kinase 3 (RIPK3)-mediated phosphorylation of mixed lineage kinase domain-like protein (pMLKL) and subsequent plasma-membrane rupture, which was demonstrated in several disease states, including ischemia–reperfusion injury (IRI) in all organs analyzed (2–6); however, none of these previous studies clearly investigated the mode of cell death in the primary parenchymal cells. Therefore, it remained possible that the protective effects reported upon application of the necroptosis inhibitor necrostatin-1 (Nec-1) and for RIPK3-ko mice involve vascular, nonparenchymal effects. This possibility has been ruled out in non-IRI settings by conditional tissue targeting of proteins involved in the prevention of spontaneously occurring necroptosis, such as RIPK1, and components that regulate its ubiquitinylation status [linear ubiquitinylation chain assembly complex (LUBAC), cellular inhibitors of apoptosis proteins (cIAPs)), caspase-8, and Fas-associated protein with death domain (FADD)] in the gastrointestinal tract (7, 8), the skin (9, 10), the liver (11), and immune cells (12, 13), all of which result in spontaneous RIPK3-mediated tissue necroptosis and inflammation (7–9, 11, 12, 14–17).

Ferroptosis is an iron-dependent necrotic type of cell death that occurs due to lipid peroxide accumulation, which routinely is prevented by glutathione peroxidase 4 (GPX4), a glutathione-(GSH)-dependent enzyme, and therefore depends on the functionality of a glu/cys antiporter in the plasma membrane referred to as system X_c^--minus (18–20). Ferroptosis has been reported to cause several diseases and may be interfered with in vitro by the small molecule ferrostatin-1 (Fer-1) (18); however, Fer-1 was suggested to have low in vivo functionality due to potential metabolic and plasma instability.

Significance

Cell death by regulated necrosis causes tremendous tissue damage in a wide variety of diseases, including myocardial infarction, stroke, sepsis, and ischemia–reperfusion injury upon solid organ transplantation. Here, we demonstrate that an iron-dependent form of regulated necrosis, referred to as ferroptosis, mediates regulated necrosis and synchronized death of functional units in diverse organs upon ischemia and other stimuli, thereby triggering a detrimental immune response. We developed a novel third-generation inhibitor of ferroptosis that is the first compound in this class that is stable in plasma and liver microsomes and that demonstrates high efficacy when supplied alone or in combination therapy.

Author contributions: A.L., T.V.B., M.B., J.M.W., C.A.R., U.K., H.-J.A., B.R.S., D.R.G., and S.K. designed research; A.L., R.S., N.H., S.R.M., C.D., F.D.Z., A.P., G.Z., F.K., T.V.B., J.M.W., J.H.B., and S.K. performed research; A.L., R.S., P.-S.W., R.W., P.V., M.P., M.B., H.-J.A., B.R.S., D.R.G., and S.K. contributed new reagents/analytic tools; A.L., R.S., N.H., S.R.M., P.-S.W., R.W., T.V.B., P.V., M.B., J.M.W., C.A.R., J.H.B., U.K., H.-J.A., B.R.S., D.R.G., and S.K. analyzed data; and A.L. wrote the paper.

The authors declare no conflict of interest.

*This Direct Submission article had a prearranged editor.

[1]To whom correspondence may be addressed. Email: andreas.linkermann@uksh.de or krautwald@nephro.uni-kiel.de.

This article contains supporting information online at www.pnas.org/lookup/suppl/doi:10.1073/pnas.1415518111/-/DCSupplemental.

In the present studies, we used inducible, conditional kidney tubule-specific genetic deletion of FADD and caspase-8, intravital microscopy, fresh isolation of primary kidney tubules, and four preclinical models of acute organ failure to further assess the relative roles of necroptosis and ferroptosis. We find that ferroptosis is of functional in vivo relevance in acute tubular necrosis and IRI, and we introduce, to our knowledge, the first ferroptosis inhibitor that is applicable for inhibition of ferroptosis in vivo. We conclude that specific combinatory therapies will be most promising for the prevention of clinically relevant IRI and that the nephron represents, to our knowledge, the first described tissue that is not sensitized to necroptosis by loss of FADD or caspase-8.

Results

Conditional Deletion of FADD or Caspase-8 Does Not Induce Cell Death in Renal Tubular Epithelia. The mode of cell death of tubular cells in acute kidney injury (AKI) has been a matter of intense discussion (21, 22). Because RIPK3-deficient mice have been shown to be partially protected from IRI-induced tubular necrosis (4, 23) and because Nec-1 phenocopies this effect (21, 24, 25), it was hypothesized that necroptosis might be the mode of cell death that drives parenchymal cells into necrosis. However, it was not ruled out that tubular cell death might have occurred secondary to some changes outside the tubular compartment: e.g., in RIPK3-dependent organ perfusion, which might be altered also upon Nec-1 treatment if the necroptotic pathway was involved. In fact, a discrepancy between the strong in vivo protection and the marginal protective effect of RIPK3-deficient freshly isolated tubules would be consistent with this hypothesis (4). A powerful approach to definitively study the involvement of cell-specific necroptosis is to delete components of the necroptosis-suppressing complex, which consists of FADD, caspase-8, RIPK1, and FLIP (26, 27), and to analyze spontaneously occurring necroptosis. We therefore crossed tubular cell-specific inducible conditional mice (Pax8-rtTA Tet-on.Cre) (28) to FADD or capase-8 floxed mice (Fig. S1 *A*–*E*) and confirmed the deficiency of the protein of interest by Western blotting from freshly isolated renal tubules (Fig. 1 *A* and *B* and *D* and *E*), which were carefully confirmed to be devoid of any other cells (Fig. S2). Unlike in all other tissues reported so far, inducible deletion of FADD or caspase-8 in Pax8-rtTA; Tet-on.Cre × FADD fl/fl and Pax8-rtTA; Tet-on.Cre × caspase-8 fl/fl mice did not affect serum markers of renal function (Fig. 1*G* and Fig. S1*F*), histological appearance (Fig. 1 *C* and *F*), or organ function for the entire observation period of 3 wk after addition of doxycyclin into the drinking water (Fig. 1*G* and Fig. S1*F*). After the 3-wk period of doxycyclin feeding, mice were morphologically indistinguishable from nondoxy-fed littermates (Fig. S1*E*). In addition, induction of acute kidney injury by application of the nephrotoxin cisplatin (20 mg/kg body weight) led to similar survival kinetics as in WT mice (Fig. 1*H*). In freshly isolated renal tubules treated with 50 μM Nec-1, no protection was detected both in the presence or in the absence of glycine (Fig. 1*I*). This result is in line with our previous observation of low levels of RIPK3 in tubular cell lines (21) and marginal sensitivity for necroptosis compared with a glomerular endothelial cell line and L929 fibrosarcoma cells (21). Taken together, these data strongly argue against necroptosis as the primary mode of regulated cell death in renal tubules and suggest that the effects in RIPK3-ko and Nec-1–treated mice are due to extratubular effects.

RIPK3-Deficient Mice Exhibit Increased Renal Perfusion and Fail To Gain Normal Body Weight. Using low-resolution intravital microscopy, we previously investigated the effects of Nec-1 on the diameter of peritubular capillaries (22). Using a similar approach with higher resolution (Fig. S3*A*), we have now analyzed RIPK3-ko mice and detected statistically significant increases in peritubular diameters (Fig. S3 *B* and *C*), which would account for 25.7% increase in blood flow (Fig. S3*D*) according to the law of Hagen Poiseuille and could help maintain peritubular perfusion after ischemia when it is known to be compromised. Taking into consideration that, in all renal cells investigated, the highest RIPK3 expression was found in endothelial cells, vascular effects cannot be ruled out, and endothelial cell-specific conditional RIPK3 depletion should be investigated in IRI models. In this respect, it is noteworthy that, in another model of necrotic parenchymal damage that does not rely on ischemia–reperfusion

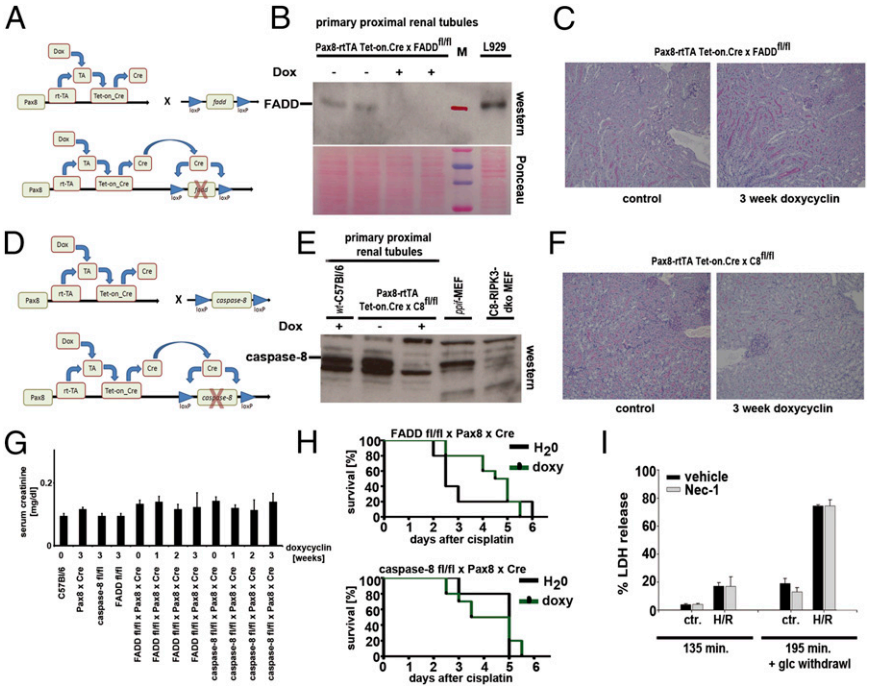

Fig. 1. Conditional deletion of FADD or caspase-8 does not sensitize renal tubules to necroptosis. (*A*) Scheme of the doxycyclin-inducible conditional tubular knockout. (*B*) After 3 wk of doxycyclin-treatment, no detection of the FADD protein in freshly isolated renal tubules was possible; L929 cells serve as a positive control. (*C*) Periodic acid–Schiff (PAS) staining of normal renal morphology in Pax8-rtA; Tet-on.Cre × FADD fl/fl mice after 3-wk treatment with doxycyclin via the drinking water. (*D*–*F*) Similarly, caspase-8 was inducibly depleted from tubules. Note that the anti-mouse monoclonal antibody against caspase-8 cross-reacts with a nonspecific protein just below the band of caspase-8. Mouse embryonic fibroblasts (MEFs) from caspase-8/RIPK3-dko mice serve as a negative control, MEFs from cyclophilin D-deficient *ppif*-ko mice serve as a positive control, as do the C57BL/6 WT mice. (*G*) Serum creatinine levels remain in the normal range in all mice investigated as indicated. (*H*) Doxycyclin-induced conditional FADD-deficient or caspase-8–deficient mice react to 20 mg/kg body weight cisplatin-induced acute kidney injury similarly to nonstimulated mice. (*I*) Necrostatin-1 (Nec-1; 50 μM) does not influence the amount of LDH released from hypoxic renal tubules, either in the presence (*Left*) or absence (*Right*) of glycine (glc) (n = 8–10 per group).

injury, the cerulein-induced pancreatitis, in our hands, RIPK3-deficient mice are not protected from the increase in serum levels of amylase and lipase (Fig. S3*E*). In addition, we noticed that RIPK3-ko mice fail to gain normal body weight in comparison with WT littermates in both males and females (Fig. S3 *F* and *G*).

Morphological Changes of Synchronized Tubular Cell Death Are Prevented by Ferrostatins. If apoptosis and necroptosis account for only minor damage of acute tubular necrosis, we asked what pathway of regulated necrosis might be causative of synchronized tubular death that we identified in an improved ex vivo model of freshly isolated murine renal tubules upon depletion of fatty acids (Fig. 2*A* and Movie S1). We confirmed such tubules to be functional before the onset of the fatty-acid depletion for maximal control purposes (Movie S2). Importantly, such synchronized tubular (cell) death very much resembles the appearance of casts found in urine sediments of patients with acute kidney injury. The dynamics of the tubular necrosis suggest a direct cell-to-cell communication to deliver the deadly signal (Movie S3). Because we previously reported a beneficial effect of the second-generation ferrostatin 11-92 (29) in a model of acute injury of freshly isolated renal tubules, we looked for the morphology of such tubules in the presence of erastin, a well-described inducer of ferroptosis, a necrotic type cell death that largely depends on lipid peroxidation (18, 19), over time (Fig. 2*B*). Whereas the

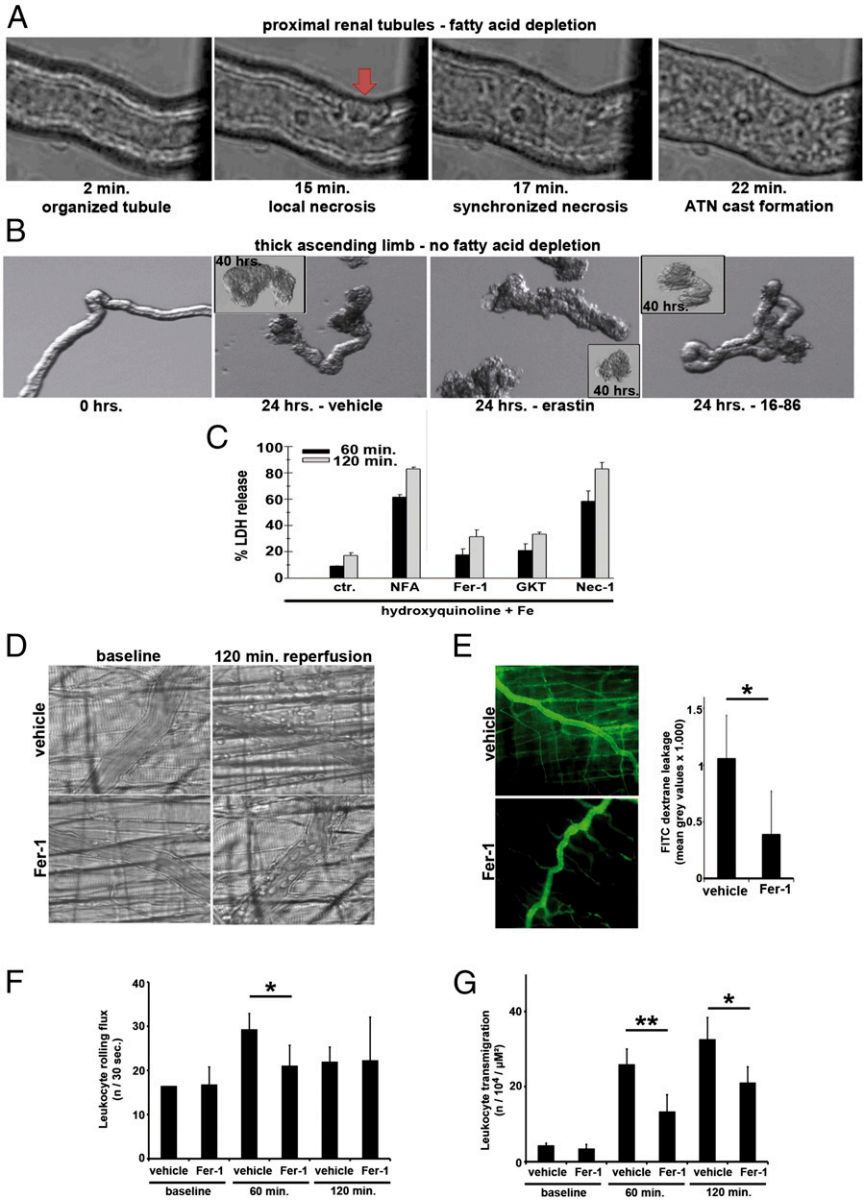

Fig. 2. Ferroptosis mediates synchronized tubular necrosis and contributes to immune-cell extravasation into ischemic tissue. (*A*) Snapshots from Movie S1 of functional freshly isolated proximal renal tubule segments undergoing rapid synchronized necrosis upon fatty-acid depletion. (*B*) In the presence of fatty acids, addition of erastin accelerated, whereas 16–86 (a third-generation ferrostatin; see Fig. 3) prevented, tubular necrosis. (*C*) During the time course of hydroxyquinoline/Fe-induced tubular necrosis, Fer-1 and the Nox-inhibitor GKT prevented LDH release whereas Nec-1 did not show protection. (*D*) Reflected light oblique transillumination imaging of leukocyte passages through postcapillary venules in IRI of the cremaster muscle in the presence of vehicle or Fer-1. (*E*) FITC dextran leakage in the same model. (*F*) Leukocyte rolling is affected by Fer-1 within the first hour after reperfusion. (*G*) Significantly reduced leukocyte transmigration in the presence of Fer-1.

faint plasma membrane of untreated tubules did not change in 16-86–treated tubules [a novel third-generation ferrostatin we generated (Fig. 3)], vehicle-treated and especially erastin-treated tubules showed membrane protrusions and obvious signs of deformation and functional insufficiency (Fig. 2*B*). When erastin was applied into the tubule, a similar type of cell death occurred even without fatty-acid depletion (Movie S4). In another well-established lactate dehydrogenase (LDH) release-based assay of ex vivo tubulotoxicity (29), hydroxyquinoline–iron-induced cell death, we found Fer-1 and the Nox-inhibitor GKT to be protective whereas Nec-1 did not show any protection (Fig. 2*C*).

Ferroptosis Mediates IRI-Mediated Immune-Cell Infiltration of the Cremaster Muscle. The concept of immunogenic necrotic cell death proposes to trigger an autoamplification loop, which is triggered by a necroinflammatory microenvironment. To understand how ferroptosis attracts immune cells during hypoxia/reperfusion situations, we performed musculus cremaster IRI assays and read out the immune-cell infiltration by intravital microscopy (Fig. 2 *D–F*) and quantified rolling, adherent, and transmigrated cells in the presence and absence of ferrostatins (Fig. 2 *F* and *G* and Fig. S4 *A* and *B*). Less immune-cell infiltration into the postischemic area suggested either that Fer-1 directly inhibits leukocyte transmigration or that the local proinflammatory microenvironment was less chemoattractive, presumably by less damage-associated molecular pattern (DAMP) release due to less ferroptotic cell death.

Ferroptosis Mediates Tubule Necrosis in Oxalate Nephropathy, but Not in an LPS-Induced Septic Shock Model. Having identified ferroptosis to be of relevance in acute postischemic injury, we sought to investigate another model of acute renal failure, oxalate nephropathy, which has recently been established (30). Intrarenal CaOx crystal deposition was identical in all groups (Fig. S5 *A* and *B*). However, neutrophil infiltration and expression levels of proinflammatory cytokines (CXCL-2, IL-6), kidney injury molecule 1 (KIM-1), and the p65 subunit of NF-κB were statistically significantly reduced upon a once daily i.p. application of Fer-1 (Fig. S5*E*). Importantly, Fer-1 also significantly reduced the tubular injury score (Fig. S5*D*) and the functional serum markers of kidney injury creatinine and urea (Fig. S5*C*). Because RIPK3-deficient mice have been demonstrated to be resistant to sepsis models, we also investigated Fer-1 in the model of LPS-induced shock (Fig. S5*F*), but no difference compared with vehicle-treated mice was evident. Therefore, ferroptosis seems to be a valuable target for both postischemic and toxic acute kidney injury. However, given the poor plasma stability of Fer-1, we sought to develop a more stable compound for the in vivo applications.

Generation of a Third-Generation Ferrostatin with Increased Plasma and Metabolic Stability for in Vivo Studies. Given the promising results of the cremaster–IRI and oxalate nephropathy studies and the previously published efficacy of second-generation ferrostatins in models of Huntington´s disease, periventricular leukomalacia, and tubular necrosis (29), we wondered whether the reported poor plasma stability of Fer-1 could be further enhanced by structure-relation analysis. We therefore first evaluated the in vitro metabolic stability of one of the highly potent Fer-1 analogs, SRS15-72B (29), in liver microsomes of mice. SRS15-72B was cleared rapidly with a half-life of $t_{1/2} = 2$ min (Table S1). To achieve a more metabolically stable Fer-1 analog, we created an imine-type structure (SRS15-72A) that showed high stability in microsomes with a half-life of $t_{1/2} = 154$ min (Table S2). This metabolically stable analog turned out not to be sufficiently stable in the plasma due to its ethyl ester moiety (Table S3), a functional group well-known to be more susceptible to hydrolysis in plasma (31). Because a previous study showed that the ethyl ester is important to maintain the potency of Fer-1, we aimed at improving the plasma stability, while maintaining high microsomal stability by creating additional imine analogs with isopropyl (SRS16-80) and *tert*-butyl (SRS16-86) esters (Fig. 3*A*). These analogs allowed us to comparatively study the plasma stability of the ethyl, isopropyl, and *tert*-butyl esters, respectively. Among these three ester analogs (SRS15-72A, SRS16-80, and SRS16-86), the *tert*-butyl ester analog (SRS16-86) showed the highest stability in plasma (Table S4). In addition, SRS16-86 maintains high stability in the microsomal compartment [intrinsic clearance (CLint) (mL/min per g liver < 0.5)] (Table S5). For in vivo experiments, we therefore used 16-86 and used it in comparison with 16–79, an inactive derivate (Fig. 3*B*). We confirmed the ferroptosis-inhibiting ability of 16-86 and 16-79 in vitro by FACS analysis of erastin-treated HT-1080 cells and in NIH 3T3 cells (Fig. 3*C*). In both necroptosis and ferroptosis, we failed to detect cleaved caspase 3 (Fig. 3*D*).

Ferroptosis Mediates Necrotic Tubular Cell Death in Renal Ischemia–Reperfusion Injury. We applied active (16-86) and inactive (16-79) compounds to a model of severe ischemia–reperfusion injury (IRI), which we described before (4). Upon 40 min of ischemia before reperfusion, we know that all WT mice die between 48 h and 72 h, which can be anticipated from the 48-h serum creatinine values above 2.0 mg/dL. As demonstrated in Fig. 4 *A–D*, creatinine levels of all vehicle-treated C57BL/6 mice exceeded 2.0 mg/dL and showed strong morphologic damage and high serum urea levels whereas Fer-1–treated and, to a greater extent,

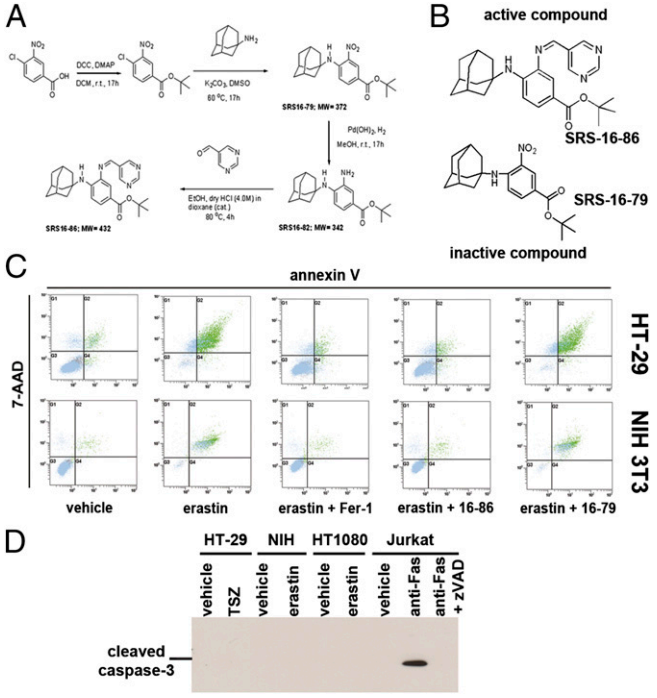

Fig. 3. Generation and in vitro testing of a ferrostatin derivative for in vivo applications. (*A*) Synthetic route of the most microsomal and plasma stable ferrostatin analog (SRS16-86). (*B*) Model structure of the two novel ferrostatin derivates SRS16-79 (inactive compound) and SRS16-86 (active compound). (*C*) FACS analysis for the necrotic marker 7AAD and phosphatidylserine accessibility (annexin V) in HT1080 and NIH 3T3 cells treated with either vehicle or 50 μM erastin in the presence or absence of 1 μM Fer-1, 16-86, or 16-79. (*D*) Absence of cleaved caspase-3 in necroptosis and ferroptosis. Western blot of cleaved caspase-3 in lysates from 100 ng/mL TNFα plus 1 μM Smac mimetics plus 25 μM zVAD-treated HT-29 cells, 50 μM erastin-treated NIH 3T3 cells, and 50 μM erastin-treated HT1080 cells for 24 h. Monoclonal anti-Fas–treated Jurkat cells (100 ng/mL) served as positive control. TSZ, TNFa/SMAC-mimetic/zVAD.

16-86–treated mice were protected from functional acute renal failure (Fig. 4 *C* and *D*) and structural organ damage (Fig. 4 *A* and *B*) after IRI. Mice treated with 16–79 in a similar manner did not show any differences compared with the vehicle-treated controls. We did not observe any side effects from treatment with the same dose of 16-86 4 wk after application. The effect of 16-86 exceeded that of any single compound we previously experienced to be protective from renal IRI.

Ferrostatins Further Increase the Protective Effect of [Necrostatin-1/Sanglifehrin A] Combination Therapy in Renal IRI. Given that Nec-1 protects from renal IRI to a lesser extent than 16-86, and given that interference with mitochondrial permeability transition (MPT)-induced regulated necrosis (MPT-RN) by the compound sanglifehrin A (SfA) also mildly protects from IRI, with marked additive protective effects in combination therapy with Nec-1 (4, 5), we sought to further extend the combination therapy by investigating the influence of 16-86 and 16-79 in [Nec-1 + SfA]-treated mice. Because the effect of the [Nec-1 + SfA] treatment could be investigated only in a severe ischemia model and we aimed to investigate additive protective effects by 16-86, we further increased the ischemic duration to a model of ultrasevere IRI (see *Materials and Methods* for details). In such settings, even the combination therapy with [Nec-1 + SfA] did not fully rescue creatinine values and organ damage (Fig. 4 *E–H*). Addition of 16-86, but not 16-79, reduced plasma levels of serum urea and serum creatinine, suggesting that a triple combination therapy with [Nec-1 + SfA] plus 16-86 is superior in the prevention of renal IRI compared with the double-combination therapy with [Nec-1 + SfA]. In addition, this result indicates either that at least three independent pathways of regulated necrosis may be involved in IR-mediated organ damage or that inhibition of overlapping elements with SfA and Nec-1 are incomplete.

Discussion

Parenchymal cell necrosis, but not apoptosis, which seems to be minimally involved in the pathogenesis of acute kidney injury (32), triggers the release of DAMPs, some of which can trigger regulated necrosis and therefore initiate a necroinflammatory feedback loop. In clinical routine, immunosuppression is a standard procedure, but an anti-cell death therapy does not exist apart from cyclosporine (5). Therefore, defining the precise mechanisms that trigger regulated necrosis is essential for the development of new drugs. Our data indicate that alternative interpretations apart from "pure" necroptosis exist and suggest that ferroptosis is of importance in renal tubules, which, other than the skin, the gastrointestinal tract, or immune cells, do not depend on a necroptosis-inhibiting complex, at least not of FADD and caspase-8. To date, it cannot be ruled out that previously described protection against ischemia–reperfusion injury in diverse organs is mediated by increased perfusion rather than direct protection from parenchymal necroptosis. Our results regarding the cerulein-induced pancreatitis are in line with this

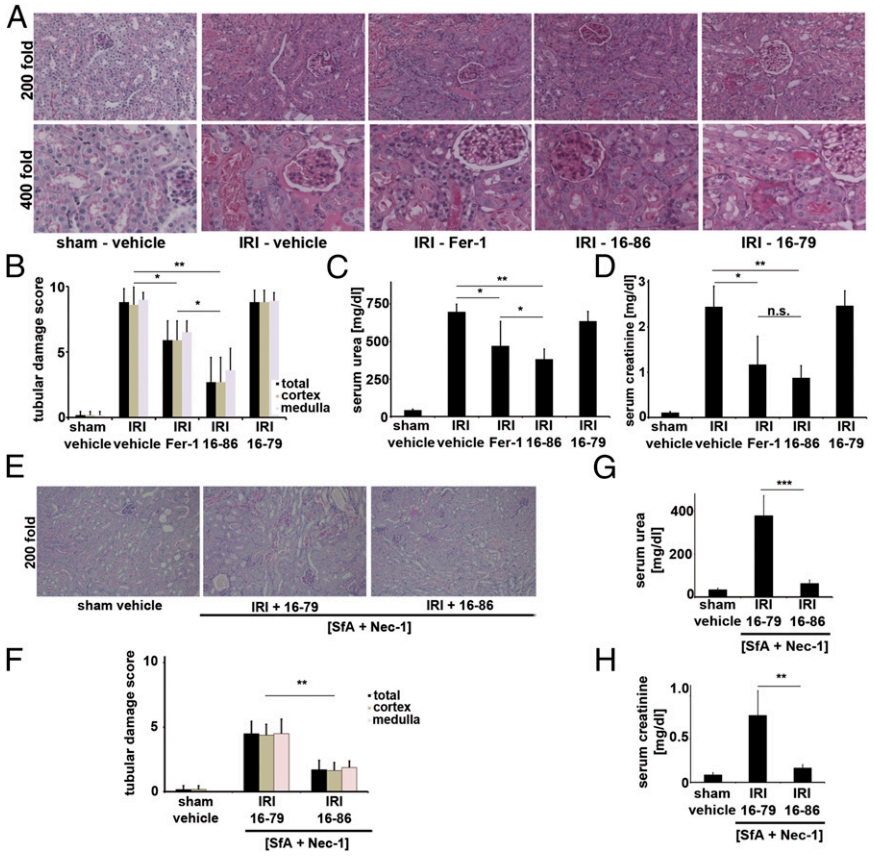

Fig. 4. Ferroptosis significantly contributes to renal ischemia–reperfusion injury. (*A* and *B*) Representative PAS stainings and quantification of renal damage from mice treated with severe ischemic durations before reperfusion. Mice were killed 48 h after reperfusion. (*C* and *D*) Functional markers of acute kidney injury after severe IRI (as in *A* and *B*). (*E* and *F*) Histologic PAS staining and quantification of sham operation or ultrasevere IRI (50 min of ischemia before reperfusion) in WT mice treated with [Nec-1 + SfA] combination therapy together with either 16-79 or 16-86. (*G* and *H*) C57BL/6 were treated as in *E*, and functional markers of acute kidney injury were measured 48 h after the onset of reperfusion. n.s., not significant; $*P = 0.05–0.02$, $**P = 0.02–0.001$, $***P \leq 0.001$; $n = 10$ per group in all experiments).

hypothesis and are in contrast to previously published data (33, 34). Several unanswered questions remain: Why are RIPK3-deficient mice protected in several models of IRI if the parenchymal cells do not undergo necroptosis? Why do necrostatins protect such tissues from organ failure if necroptosis is not the predominant mechanism of parenchymal cell death? Endothelial cell-specific deletion of RIPK3 will help to answer these open questions.

Materials and Methods

See *SI Materials and Methods* for detailed descriptions.

Mice. All WT mice reported in this study were on C57BL/6 background. Eight- to 12-wk-old male C57BL/6 mice (average weight ~23 g) were used for all WT experiments, unless otherwise specified. Caspase-8 fl/fl mice were kindly provided by Razquella Hakem (Department of Medical Biophysics, University of Toronto, Toronto and Ontario Cancer Institute, University Health Network, Toronto). FADD fl/fl mice were generated by and provided by M.P. Doxycyclin-inducible renal tubule-specific Pax8-rtTA; Tet-on.Cre mice have been published (28) and were kindly provided by Tobias B. Huber (Renal Division, University Medical Center Freiburg, Freiburg, Germany). RIPK3-deficient mice were kindly provided by Vishva M. Dixit (Genentech, San Francisco, CA). All in vivo experiments were performed according to the Protection of Animals Act, after approval of the German local authorities or the Institutional Animal Care and Use Committee (IACUC) of the University of Michigan, and the National Institutes of Health *Guide for the Care and Use of Laboratory Animals* (35), after approval from the University of Michigan IACUC or by the local authorities responsible for the approval at Ghent University. In all experiments, mice were carefully matched for age, sex, weight, and genetic background.

Histology, Immunohistochemistry, and Evaluation of Structural Organ Damage. Organs were dissected as indicated in each experiment and infused with 4% (vol/vol) neutral-buffered formaldehyde, fixated for 48 h, dehydrated in a graded ethanol series and xylene, and finally embedded in paraffin. Stained sections were analyzed using an Axio Imager microscope (Zeiss). Kidney damage was quantified by two experienced pathologists in a double-blind manner on a scale ranging from 0 (unaffected tissue) to 10 (severe organ damage). The following parameters were chosen as indicative of morphological damage to the kidney after ischemia–reperfusion injury (IRI): brush border loss, red blood cell extravasation, tubule dilatation, tubule degeneration, tubule necrosis, and tubular cast formation. These parameters were evaluated on a scale of 0–10, which ranged from not present (0), mild (1–4), moderate (5 or 6), severe (7 or 8), to very severe (9 or 10). Each parameter was determined on at least four different animals.

Statistics. For all experiments, differences of datasets were considered statistically significant when P values were lower than 0.05, if not otherwise specified. Statistical comparisons were performed using the two-tailed Student t test. Asterisks are used in the figures to specify statistical significance ($*P < 0.05$; $**P < 0.02$; $***P < 0.001$). P values in survival experiments (Kaplan–Meier plots) were calculated using GraphPad Prism, ver. 5.04 software. Statistics are indicated as SD unless otherwise specified.

ACKNOWLEDGMENTS. We thank Katja Bruch, Maike Berger, Janina Kahl, and Monika Iversen for excellent technical assistance and Justus Cordt for expert help with mouse weight charts. A.L. received funding from the German Society for Nephrology, the Else Kröner-Fresenius Stiftung, Pfizer, and Novartis. H.-J.A. is supported by Deutsche Forschungsgemeinschaft Grants AN372/9-2, AN371/12-2, and AN372/15-1 and the Else Kröner-Fresenius Stiftung. B.R.S. is an Early Career Scientist of the Howard Hughes Medical Institute and received funding from New York State Stem Cell Science (Contract C026715 for the Chemical Probe Synthesis Facility), the US National Institutes of Health (NIH Grants R01CA097061, R01GM085081, and R01CA161061), the Whitehall Foundation, the William Randolph Hearst Foundation, and the Baby Alex Foundation. J.M.W. is supported by NIH Grant R01DK34275 and the Veterans Administration. Research in the P.V. unit is supported by Belgian grants (Interuniversity Attraction Poles Grants IAP 6/18 and IAP 7/32), Flemish grants (Research Foundation Flanders Grants FWO G.0875.11, FWO G.0973.11 N, FWO G.0A45.12 N, FWO G.0172.12, FWO G.0787.13N, G0C3114N, and FWO KAN 31528711), Ghent University grants (Multidisciplinary Research Partnership, Ghent Researchers On Unfolded Proteins in Inflammatory Disease consortium), and grants from the Flanders Institute for Biotechnology. P.V. holds Methusalem Grant BOF09/01M00709 from the Flemish Government. S.K. received grants from Pfizer, Novartis, Fresenius, and the Else Kröner-Fresenius Stiftung.

1. Galluzzi L, Kepp O, Krautwald S, Kroemer G, Linkermann A (2014) Molecular mechanisms of regulated necrosis. *Semin Cell Dev Biol* 35C:24–32.
2. Kaczmarek A, Vandenabeele P, Krysko DV (2013) Necroptosis: The release of damage-associated molecular patterns and its physiological relevance. *Immunity* 38(2): 209–223.
3. Vanden Berghe T, Linkermann A, Jouan-Lanhouet S, Walczak H, Vandenabeele P (2014) Regulated necrosis: The expanding network of non-apoptotic cell death pathways. *Nat Rev Mol Cell Biol* 15(2):135–147.
4. Linkermann A, et al. (2013) Two independent pathways of regulated necrosis mediate ischemia-reperfusion injury. *Proc Natl Acad Sci USA* 110(29):12024–12029.
5. Linkermann A, Green DR (2014) Necroptosis. *N Engl J Med* 370(5):455–465.
6. Linkermann A, et al. (2013) Necroptosis in immunity and ischemia-reperfusion injury. *Am J Transplant* 13(11):2797–2804.
7. Günther C, et al. (2011) Caspase-8 regulates TNF-α-induced epithelial necroptosis and terminal ileitis. *Nature* 477(7364):335–339.
8. Welz PS, et al. (2011) FADD prevents RIP3-mediated epithelial cell necrosis and chronic intestinal inflammation. *Nature* 477(7364):330–334.
9. Bonnet MC, et al. (2011) The adaptor protein FADD protects epidermal keratinocytes from necroptosis in vivo and prevents skin inflammation. *Immunity* 35(4):572–582.
10. Gerlach B, et al. (2011) Linear ubiquitination prevents inflammation and regulates immune signalling. *Nature* 471(7340):591–596.
11. Liedtke C, et al. (2011) Loss of caspase-8 protects mice against inflammation-related hepatocarcinogenesis but induces non-apoptotic liver injury. *Gastroenterology* 141(6):2176–2187.
12. Osborn SL, et al. (2010) Fas-associated death domain (FADD) is a negative regulator of T-cell receptor-mediated necroptosis. *Proc Natl Acad Sci USA* 107(29):13034–13039.
13. Wong WW, et al. (2014) cIAPs and XIAP regulate myelopoiesis through cytokine production in an RIPK1- and RIPK3-dependent manner. *Blood* 123(16):2562–2572.
14. Ch'en IL, et al. (2008) Antigen-mediated T cell expansion regulated by parallel pathways of death. *Proc Natl Acad Sci USA* 105(45):17463–17468.
15. Kaiser WJ, et al. (2011) RIP3 mediates the embryonic lethality of caspase-8-deficient mice. *Nature* 471(7338):368–372.
16. Oberst A, et al. (2011) Catalytic activity of the caspase-8-FLIP(L) complex inhibits RIPK3-dependent necrosis. *Nature* 471(7338):363–367.
17. Zhang H, et al. (2011) Functional complementation between FADD and RIP1 in embryos and lymphocytes. *Nature* 471(7338):373–376.
18. Dixon SJ, et al. (2012) Ferroptosis: An iron-dependent form of nonapoptotic cell death. *Cell* 149(5):1060–1072.
19. Yagoda N, et al. (2007) RAS-RAF-MEK-dependent oxidative cell death involving voltage-dependent anion channels. *Nature* 447(7146):864–868.
20. Yang WS, et al. (2014) Regulation of ferroptotic cancer cell death by GPX4. *Cell* 156(1-2):317–331.
21. Linkermann A, et al. (2012) Rip1 (receptor-interacting protein kinase 1) mediates necroptosis and contributes to renal ischemia/reperfusion injury. *Kidney Int* 81(8):751–761.
22. Linkermann A, et al. (2013) The RIP1-kinase inhibitor necrostatin-1 prevents osmotic nephrosis and contrast-induced AKI in mice. *J Am Soc Nephrol* 24(10):1545–1557.
23. Luedde M, et al. (2014) RIP3, a kinase promoting necroptotic cell death, mediates adverse remodelling after myocardial infarction. *Cardiovasc Res* 103(2):206–216.
24. Degterev A, et al. (2005) Chemical inhibitor of nonapoptotic cell death with therapeutic potential for ischemic brain injury. *Nat Chem Biol* 1(2):112–119.
25. Smith CC, et al. (2007) Necrostatin: A potentially novel cardioprotective agent? *Cardiovasc Drugs Ther* 21(4):227–233.
26. Dillon CP, et al. (2012) Survival function of the FADD-CASPASE-8-cFLIP(L) complex. *Cell Reports* 1(5):401–407.
27. Dillon CP, et al. (2014) RIPK1 blocks early postnatal lethality mediated by caspase-8 and RIPK3. *Cell* 157(5):1189–1202.
28. Traykova-Brauch M, et al. (2008) An efficient and versatile system for acute and chronic modulation of renal tubular function in transgenic mice. *Nat Med* 14(9): 979–984.
29. Skouta R, et al. (2014) Ferrostatins inhibit oxidative lipid damage and cell death in diverse disease models. *J Am Chem Soc* 136(12):4551–4556.
30. Mulay SR, et al. (2013) Calcium oxalate crystals induce renal inflammation by NLRP3-mediated IL-1β secretion. *J Clin Invest* 123(1):236–246.
31. Di L, Kerns EH, Hong Y, Chen H (2005) Development and application of high throughput plasma stability assay for drug discovery. *Int J Pharm* 297(1-2):110–119.
32. Linkermann A, et al. (2014) Regulated Cell Death in AKI. *J Am Soc Nephrol*, ASN.2014030262.
33. He S, et al. (2009) Receptor interacting protein kinase-3 determines cellular necrotic response to TNF-alpha. *Cell* 137(6):1100–1111.
34. Zhang DW, et al. (2009) RIP3, an energy metabolism regulator that switches TNF-induced cell death from apoptosis to necrosis. *Science* 325(5938):332–336.
35. National Research Council (2011) *Guide for the Care and Use of Laboratory Animals* (National Academies Press, Washington, DC), 8th Ed.

Supporting Information

Linkermann et al. 10.1073/pnas.1415518111

SI Materials and Methods

Mice. All WT mice (C57BL/6) reported in this study were obtained from Charles River. Eight- to 12-wk-old male C57BL/6 mice (average weight ∼23 g) were used for all WT experiments, unless otherwise specified. Caspase-8 fl/fl mice were kindly provided by Razquella Hakem (Department of Medical Biophysics, University of Toronto, Toronto and Ontario Cancer Institute, University Health Network, Toronto). FADD fl/fl mice were generated by and provided by M.P. Doxycyclin-inducible renal tubule-specific Pax8-rtTA; Tet-on.Cre mice have been published (1) and were kindly provided by Tobias B. Huber (Renal Division, University Medical Center Freiburg, Freiburg, Germany). RIPK3-deficient mice were kindly provided by Vishva M. Dixit. All in vivo experiments were performed according to the Protection of Animals Act, after approval of the German local authorities or the Institutional Animal Care and Use Committee (IACUC) of the University of Michigan, and the National Institutes of Health *Guide for the Care and Use of Laboratory Animals* (2), after approval from the University of Michigan IACUC or by the Local authorities responsible for the approval at Ghent University. In all experiments, mice were carefully matched for age, sex, weight, and genetic background. Genotypes were confirmed by tail-snip PCR using the following primers: Pax8-rtTA forward, 5′-CCATGTCTAGACTGGACAAGA-3′; Pax8-rtTA reverse, 5′-CTCCAGGCCACATATGATTAG-3′; tetO-Cre forward, 5′-GCATTACCGGTCGATGCAACGAGTGATGAG-3′; tetO-Cre reverse,5′-GAGTGAACGAACCTGGTCGAAATCAGTGCG-3′; caspase-8 flox/flox forward, 5′-ATAATTCCCCCAAATCCTCGCATC-3′; caspase-8 flox/flox reverse,5′-GGCTCACTCCCAGGGCTTCCT-3′; FADD flox/flox forward, 5′-TCACCGTTGCTCTTTGTCTAC-3′; FADD flox/flox reverse (I), 5′-GTAATCTCTGTAGGGAGCCCT-3′; and FADD flox/flox reverse (II), 5′-CTAGCGCATAGGATGATCAGA-3′.

Cell Lines and Reagents. Necrostatin (Nec-1) was obtained from Sigma-Aldrich. Sanglifehrin A (SfA) was provided by Novartis Pharma. The zVAD-fmk (herein referred to as zVAD) was purchased from BD Biosciences. The monoclonal anti-Fas antibody was from Immunotech. Smac mimetics (Birinapant) was from Absource Diagnostics (Selleckchem). Murine NIH 3T3 fibroblasts were originally obtained from ATCC and were cultured in Dulbecco's modified Eagle medium (DMEM) (Invitrogen) supplemented with 10% (vol/vol) FCS, 100 U/mL penicillin, and 100 μg/mL streptomycin. Human HT-1080 fibrosarcoma cells were originally obtained from ATCC and were cultured in DMEM (Invitrogen) supplemented with MEM NEAA (Invitrogen), 10% (vol/vol) FCS, 100 U/mL penicillin, and 100 μg/mL streptomycin. Murine NIH 3T3 cells were originally obtained from ATCC and were cultured in DMEM (Invitrogen) supplemented with 10% (vol/vol) FCS, 100 U/mL penicillin, and 100 μg/mL streptomycin. Jurkat cells were originally obtained from ATCC and were cultured in RPMI 1640 supplemented with 10% (vol/vol) FCS, 100 U/mL penicillin, and 100 μg/mL streptomycin. All cell lines were cultured in a humidified 5% CO_2 atmosphere.

Induction of Cell Death. For induction of necroptosis, HT-29 cells were stimulated for 24 h at 37 °C with 100 ng/mL TNFα plus 1 μM Smac mimetics plus 25 μM zVAD as indicated (vehicle-treated cells served as control). For induction of ferroptosis, NIH and HT-1080 cells were each stimulated for 24 h at 37 °C with 50 μM erastin as indicated (vehicle-treated cells served as control). For induction of apoptosis, Jurkat cells were stimulated for 4 h with 100 ng/mL monoclonal anti-Fas (clone 7C11; Immunotech). Anti-Fas–induced apoptosis of Jurkat cells was inhibited by further addition of 25 μM zVAD (vehicle-treated cells served as control).

Analysis of Cell Death. For immunoblotting, cells were lysed in ice-cold 10 mM Tris·HCl, pH7.5, 50 mM NaCl, 1% Triton X-100, 30 mM sodium pyrophosphate, 50 mM NaF, 100 μM Na_3VO_4, 2 μM $ZnCl_2$, and 1 mM phenylmethylsulfonyl fluoride (modified Frackelton buffer). Insoluble material was removed by centrifugation (14,000 × *g*, 10 min, 4 °C), and protein concentration was determined using a commercial Bradford assay kit according to the manufacturer's instructions (Bio-Rad).

Equal amounts of protein (17 μg per lane) were resolved on a 12% SDS/PAGE gel and transferred to a nitrocellulose membrane (Amersham Biosciences). Western blot was performed using a polyclonal cleaved caspase-3 antibody (Asp-175 from Cell Signaling) and a corresponding secondary horseradish peroxidase-linked polyclonal anti-rabbit antibody (Acris). Immune complexes were visualized by enhanced chemiluminescence (ECL; Amersham Biosciences).

Fluorescence-Activated Cell Sorting. Phosphatidylserine exposure to the outer cell membrane of apoptotic cells or at the inner plasma membrane of necrotic cells and incorporation of 7-AAD into necrotic cells were quantified by fluorescence-activated cell sorting (FACS) analysis. The ApoAlert annexin V-FITC antibody and the 7-AAD antibody were purchased from BD Biosciences.

Isolation of Renal Tubules. Six to 12 mice were used for each isolated tubule preparation, depending on the amount of material needed for particular experiments. For preparation of isolated tubules, mice were anesthetized with ketamine (100 mg/kg i.p.) and xylazine (10 mg/kg i.p.), and the kidneys were immediately removed. Type I collagenase was from Worthington Biochemical. Percoll was purchased from Amersham Biosciences. All other reagents and chemicals, including delipidated BSA, were of the highest grade available from Sigma-Aldrich. Immediately after removal of the kidneys, the parenchyma was injected with 0.3–0.5 cc of a cold 95% O_2/5% CO_2-gassed solution consisting of 115 mM NaCl, 2.1 mM KCl, 25 mM $NaHCO_3$, 1.2 mM KH_2PO_4, 2.5 mM $CaCl_2$, 1.2 mM $MgCl_2$, 1.2 mM $MgS0_4$, 25 mM mannitol, 2.5 mg/mL fatty acid-free BSA, 5 mM glucose, 4 mM sodium lactate, 1 mM alanine, and 1 mM sodium butyrate (solution A) with the addition of 1 mg/mL collagenase (type I; Worthington Biochemical). The cortices were then dissected and minced on an ice-cold tile and then resuspended in additional solution A for 8–10 min of digestion at 37 °C, followed by enrichment of proximal tubules using centrifugation on self-forming Percoll gradients. For Nec-1 studies in renal tubules, renal cortices were dissected in ice-cold dissection solution (DS) [HBSS with 10 mmol/L glucose, 5 mmol/L glycine, 1 mmol/L alanine, 15 mmol/L Hepes (pH 7.4); osmolality, 325 mOsmol/L] and sliced into 1-mm pieces. The fragments were transferred to collagenase solution [DS with 0.1% (wt/vol) type 2 collagenase and 96 μg/mL soybean trypsin inhibitor] and digested for 30 min at 37 °C and 61 × *g*. After digestion, the supernatant was sieved through two nylon sieves: first 250-μm pore size and then 100-μm pore size. The longer proximal tubule segments remaining in the 100-μm sieve were resuspended by flushing the sieve in the reverse direction with warm DS (37 °C) containing BSA 1% (wt/vol). The proximal tubule suspension was

centrifuged for 5 min at 170 × *g*, washed, and then resuspended into the appropriated amount of culture medium (1:1 DMEM/F12 without phenol red and supplemented with heat-inactivated 1% FCS, 15 mmol/L Hepes, 2 mmol/L L-glutamine, 50 nmol/L hydrocortisone, 5 μg/mL insulin, 5 μg/mL transferrin, 5 ng/mL sodium selenite, 0.55 mmol/L sodium pyruvate, 10 mL/L 100× nonessential amino acids, 100 IU/mL penicillin, and 100 μg/mL streptomycin buffered to pH 7.4 (osmolality of 325 mOsmol/kg H_2O). The proximal tubule fragments were seeded onto a tissue-culture plate and cultured at 37 °C and 95% air/5% CO_2 in a standard humidified incubator.

Experimental Procedures for, and Movies of, Freshly Isolated Tubules. Incubation conditions were similar to those used previously for mouse tubule studies (3). Tubules were suspended at 2.0–3.0 mg of tubule protein per milliliter in a 95% air/5% CO_2-gassed medium containing 110 mM NaCl, 2.6 mM KCl, 25 mM $NaHCO_3$, 2.4 mM KH_2PO_4, 1.25 mM $CaCl_2$, 1.2 mM $MgCl_2$, 1.2 mM $MgSO_4$, 5 mM glucose, 4 mM sodium lactate, 0.3 mM alanine, 5 mM sodium butyrate, 2 mM glycine, and 1.0 mg/mL bovine gelatin (75 bloom) (solution B). For studies comparing normoxia with hypoxia/reoxygenation, at the end of the 15 min, preincubation tubules were resuspended in fresh solution B and regassed with either 95% air/5% CO_2 (normoxic controls) or 95% N_2/5% CO_2 (hypoxia). During hypoxia, solution B was kept at pH 6.9 to simulate tissue acidosis during ischemia in vivo, and the usual substrates (glucose, lactate, alanine, and butyrate) were omitted. After 30 min, samples were removed for analysis. The remaining tubules were pelleted and then resuspended in fresh 95% air/ 5% CO_2-gassed, pH 7.4 solution B with experimental agents as needed. Sodium butyrate in solution B was replaced with 2 mM heptanoic acid during reoxygenation and supplemented with 250 μM AMP, 0.5 mg/dL delipidated albumin, and 4 mM each α-ketoglutarate and malate. After 60 min of reoxygenation, tubules were sampled for studies. Movies with perfused isolated tubules recorded in the presence and absence of fatty acids as indicated were taken from C57BL/6 mice, which were killed under deep isoflurane anesthesia by decapitation. Kidneys were removed immediately, sliced, and transferred into incubation buffer (140 mmol/L NaCl, 0.4 mmol/L KH_2PO_4, 1.6 mmol/L K_2HPO_4, 1 mmol/L $MgSO_4$, 10 mmol/L Na-acetate, 1 mmol/L α-ketoglutarate, 1.3 mmol/L Ca-gluconate, and 5 mmol/L glycine, containing 48 mg/L trypsin inhibitor and 25 mg/L DNase I at pH 7.4). Proximal tubules (PTs) were isolated mechanically and transferred into the bath on a heated microscope stage [Axiovert 10 (PT1) or Axiovert 35M]. Tubules were held by a concentric glass pipette system. The rates of tubular perfusion via the micropipette were 10–20 nL/min. The bath was thermostatted at 37 °C, and continuous bath perfusion at 3–5 mL/min was obtained by gravity perfusion. PTs were monitored by a digital imaging system (Visitron Systems GmbH) and analyzed by MetaFluor software. Brightfield images were obtained every 10–20 s and stored for off-line analysis. Solution I (140 mmol/L NaCl, 0.4 mmol/L KH_2PO_4, 1.6 mmol/L K_2HPO_4, 1 mmol/L $MgCl_2$, 5 mmol/L glucose, 1.3 mmol/L Ca-gluconate, at pH 7.4) was used for fatty-acid depletion, and Solution II (140 mmol/L NaCl, 0.4 mmol/L KH_2PO_4, 1.6 mmol/L K_2HPO_4, 1 mmol/L $MgSO_4$, 1.3 mmol/L Ca-gluconate, 10 mmol/L Na-acetate, 1 mmol/L α-ketoglutarate, 5 mmol/L glycine, and 5 mmol/L glucose, at pH 7.4) was used for adapted PT substrate supply.

In Vivo Microscopy on the Postischemic Cremaster Muscle. The surgical preparation of the cremaster muscle was performed as originally described by Baez with minor modifications (1, 4). Mice were anesthetized using a ketamine/xylazine mixture (100 mg/kg ketamine and 10 mg/kg xylazine), administrated by i.p. injection. The left femoral artery was cannulated in a retrograde manner for administration of microspheres and drugs. The right cremaster muscle was exposed through a ventral incision of the scrotum. The muscle was opened ventrally in a relatively avascular zone, using careful electrocautery to stop any bleeding, and spread over the transparent pedestal of a custom-made microscopic stage. Epididymis and testicle were detached from the cremaster muscle and placed into the abdominal cavity. Throughout the procedure as well as after surgical preparation during in vivo microscopy, the muscle was superfused with warm-buffered saline.

The setup for in vivo microscopy was centered around an Olympus BX 50 upright microscope (Olympus Microscopy), equipped for stroboscopic fluorescence epiillumination microscopy. Light from a 75-W xenon source was narrowed to a near-monochromatic beam of a wavelength of 700 nm by a galvanometric scanner (Polychrome II; TILL Photonics) and directed onto the specimen via an FITC filter cube equipped with dichroic and emission filters (DCLP 500, LP515; Olympus). Microscopy images were obtained with Olympus water immersion lenses [20×/numerical aperture (N.A.) 0.5 and 10×/N.A. 0.3] and recorded with an analog black-and-white charge-coupled device (CCD) video camera (Cohu 4920; Cohu) and an analog video recorder (AG-7350-E; Panasonic). Oblique illumination was obtained by positioning a mirroring surface (reflector) directly below the specimen and tilting its angle relative to the horizontal plane. The reflector consisted of a round cover glass (thickness, 0.19–0.22 mm; diameter, 11.8 mm), which was coated with aluminum vapor (Freichel) and brought into direct contact with the overlying specimen as described previously (4). For measurement of centerline blood flow velocity, green fluorescent microspheres (2-μm diameter; Molecular Probes) were injected via the femoral artery catheter, and their passage through the vessels of interest was recorded using the FITC filter cube under appropriate stroboscopic illumination (exposure, 1 ms; cycle time, 10 ms; length of the electromagnetic wave, 488 nm), integrating video images for sufficient time (>80 ms) to allow for the recording of several images of the same bead on one frame. Beads that were flowing freely along the centerline of the vessels were used to determine blood-flow velocity.

For off-line analysis of parameters describing the sequential steps of leukocyte extravasation, we used the Cap-Image image analysis software (Dr. Zeintl Biomedical Engineering). Rolling leukocytes were defined as those moving slower than the associated blood flow and were quantified as described previously (4). Firmly adherent cells were determined as those resting in the associated blood flow for more than 30 s and related to the luminal surface per 100-μm vessel length. Transmigrated cells were counted in regions of interest (ROI), covering 75 μm on both sides of a vessel over a 100-μm vessel length. By measuring the distance between several images of one fluorescent bead under stroboscopic illumination, centerline blood-flow velocity was determined. From measured vessel diameters and centerline blood-flow velocity, apparent wall-shear rates were calculated, assuming a parabolic flow-velocity profile over the vessel cross-section.

Animals were treated with ferrostatin-1 (2 mg/kg i.p.) or vehicle 30 min before the experiment. For the analysis of postischemic leukocyte responses, three postcapillary vessel segments in a central area of the spread-out cremaster muscle were randomly chosen. After having obtained baseline recordings of leukocyte rolling, firm adhesion, and transmigration in all three vessel segments, ischemia was induced by clamping all supplying vessels at the base of the cremaster muscle using a vascular clamp (Martin). After 30 min of ischemia, the vascular clamp was removed, and reperfusion was restored for 160 min. Measurements were repeated at 60 min and 120 min after onset of reperfusion. Subsequently, FITC dextran was infused intraarterial (i.a.) for the analysis of microvascular permeability. After in vivo microscopy, blood samples were collected by cardiac puncture for the determination of systemic leukocyte counts using a Coulter AcT Counter (Coulter). Anesthetized animals were then euthanized by exsanguination.

Analysis of microvascular permeability was performed as described previously (3). Briefly, the macromolecule FITC-dextran (5 mg in 0.1 mL saline, M_r 150,000; Sigma-Aldrich) was infused i.a. after determination of centerline blood-flow velocity. Five postcapillary vessel segments, as well as the surrounding perivascular tissue, were excited at 488 nm, and emission >515 nm was recorded by a CCD camera (Sensicam; PCO) 30 min after injection of FITC-dextran using an appropriate emission filter (LP 515). Mean gray values of fluorescence intensity were measured by digital image analysis (TILLvisION 4.0; TILL Photonics) in six randomly selected ROIs (50×50 μm^2), localized 50 μm distant from the postcapillary venule under investigation. The average of mean gray values was calculated.

Acute Oxalate Nephropathy Model. Mice were divided into two groups. One group received vehicle injections and another group received Ferrostatin-1 (10 mg/kg i.p.). Then, 15 min later, both groups were given a single i.p. injection of 100 mg/kg sodium oxalate and 3% sodium oxalate in drinking water. Blood samples and kidneys were harvested after 24 h. Kidneys were kept at –80 °C for protein isolation and at –20 °C for RNA isolation. One part of the kidney was also kept in formalin to be embedded in paraffin for histological analysis. Kidney sections (2 μm) were stained with periodic acid–Schiff (PAS) reagent. Tubular injury was scored by assessing the percentage of necrotic tubules. Ly6B.2+ neutrophils were identified by immunostaining (clone 7/4; Serotec). Pizzolato stain was used to visualize CaOx crystals, and crystal deposit formation in the kidney was evaluated as described previously (4), using the following point values: 0, no deposits; 1, crystals in papillary tip; 2, crystals in cortical medullary junction; 3, crystals in cortex. When crystals were observed in multiple areas, points were combined. Serum creatinine and blood urea nitrogen were measured using Creatinine FS kit and Urea FS kit (both from DiaSys Diagnostic Systems) according to the manufacturer's protocol. Neutrophil infiltrates were counted in 15 high-power fields (hpfs) per section. For real-time quantitative RT-PCR, total RNA was isolated from kidneys using a Qiagen RNA extraction kit following the manufacturer's instructions. After quantification, RNA quality was assessed using agarose gels. From isolated RNA, cDNA was prepared using reverse transcriptase (Superscript II; Invitrogen). Real-time quantitative RT-PCR (TaqMan) was performed using SYBR-Green PCR master mix and analyzed with a Light Cycler 480 (Roche). All gene expression values were normalized using 18S RNA as a housekeeping gene. All primers used for amplification were from Metabion. The expression of KIM-1, IL-6, CXCL-2, and NF-κB p65 was analyzed using the following primers: Kim-1 forward, TCAGCTCGGGAATGCACA; Kim-1 reverse, TGGTTGCCTTCCGTGTCT; IL-6 forward, TGATGCACTTGCAGAAAACA; IL-6 reverse, ACCAGAGGAAATTTTCAATAG; CXCL-2 forward, TCCAGGTCAGTTAGCCTTGC; CXCL-2 reverse, CGGTCAAAAAGTTTGCCTTG; NF-κB p65 forward, CGCTTCTCTTCAATCCGGT; NF-κB p65 reverse, GAGTCTCCATGCAGCTACGG.

Kidney Model of Ischemia–Reperfusion Injury. Induction of kidney IRI was performed via a midline abdominal incision and a bilateral renal pedicle clamping for either 40 min (severe IRI, or "lethal-to-WT" IRI) or 50 min (ultra-severe IRI) using microaneurysm clamps (Aesculab). Throughout the surgical procedure, the body temperature was maintained between 36 °C and 37 °C by continuous monitoring using a temperature-controlled self-regulated heating system (Fine Science Tools). After removal of the clamps, reperfusion of the kidneys was confirmed visually. The abdomen was closed in two layers using standard 6-0 sutures. Sham-operated mice underwent the identical surgical procedures, except that microaneurysm clamps were not applied. To maintain fluid balance, all of the mice were supplemented with 1 mL of prewarmed PBS administered intraperitoneally directly after surgery. All mice were killed 48 h after reperfusion for each experiment. For assays investigating combination therapy with [Nec-1 + SfA], mice received a total volume of 150 μL of Clinoleic with 10 mg of SfA per kg of body weight and 1.65 mg of Nec-1 per kg body weight 60 min before ischemia. Then, 2 mg of 16-86 or 16-79 per kg body weight were dissolved in 2% DMSO and were applied intraperitoneally as a total volume of 400 μL 15 min before the onset of surgery in all experiments. All ischemia–reperfusion experiments were performed in a double-blinded manner.

Model of Cerulein-Induced Pancreatitis. Cerulein-induced pancreatitis (CIP) has been described elsewhere in detail (3). Briefly, male C57BL/6 WT mice ($n = 7$) and male RIPK3-ko mice ($n = 7$) received i.p. injections of 50 μg cerulein/kg body weight once every hour for 10 h (in each case, 200 μL of total volume supplemented with PBS). Animals were euthanized 24 h after the first injection, and samples of blood and tissues were rapidly harvested. Quantification of pancreas injury was performed by measuring serum amylase and lipase activity.

LPS-Induced Lethal Shock. Mice were injected intraperitoneally (i.p.) with 15 mg/kg *Escherichia coli* O111:B4 LPS (Sigma-Aldrich). Mice were pretreated by an i.p. injection of 5 mg/kg ethyl 3-amino-4-(cyclohexylamino)benzoate (Fer-1; Matrix Scientific), 10 mg/kg [5-((7-Cl-1H-indol-3-yl)methyl)-3-methylimidazolidine-2,4-dione] (Nec-1s; synthesized in house), a combination of Fer-1 and Nec-1s, or vehicle (1% DMSO in PBS) 30 min before the LPS challenge. Rectal body temperature and survival rates were monitored daily up to 96 h. Experiments were approved by the animal ethics committee of Ghent University.

Histology, Immunohistochemistry, and Evaluation of Structural Organ Damage. Organs were dissected as indicated in each experiment and infused with 4% neutral-buffered formaldehyde, fixated for 48 h, dehydrated in a graded ethanol series and xylene, and finally embedded in paraffin. Paraffin sections (3–5 μm) were stained with periodic acid–Schiff (PAS) reagent, according to standard routine protocol. Stained sections were analyzed using an Axio Imager microscope (Zeiss) at 200× or 400× magnification. Micrographs were digitalized using an AxioCam MRm Rev. 3 FireWire camera and AxioVision ver. 4.5 software (Zeiss). Organ damage was quantified by two experienced pathologists in a double-blind manner on a scale ranging from 0 (unaffected tissue) to 10 (severe organ damage). For the scoring system, tissues were stained with PAS, and the degree of morphological involvement in renal failure was determined using light microscopy. The following parameters were chosen as indicative of morphological damage to the kidney after ischemia–reperfusion injury (IRI): brush border loss, red blood cell extravasation, tubule dilatation, tubule degeneration, tubule necrosis, and tubular cast formation. These parameters were evaluated on a scale of 0–10, which ranged from not present (0), mild (1–4), moderate (5 or 6), severe (7 or 8), to very severe (9 or 10). Each parameter was determined on at least four different animals.

General Procedures for the Synthesis of Ferrostatin-1 and Derivatives. ***General Information.*** Concerning chemicals generally, solvents, inorganic salts, and organic reagents were purchased from commercial sources such as Sigma and Fisher and used without further purification unless otherwise mentioned. For chromatography, Merck precoated 0.25-mm silica plates containing a 254-nm fluorescence indicator were used for analytical TLC. Flash chromatography was performed on 230–400 mesh silica (SiliaFlash P60) from Silicycle. For spectrometry, ^1H, and ^{13}C NMR spectra were obtained on a Bruker DPX 400 MHz spectrometer. High-resolution mass spectrometry (HRMS) spectra

were taken on a double-focusing sector-type mass spectrometer (HX-110A; JEOL Ltd.) [resolution of 10,000 and 10 kV acceleration voltage ionization method, fast atom bombardment (FAB), Xe 3 kV energy, matrix NBA (m-nitrobenzyl alcohol)].

General procedure A (tert-butyl ester formation). To the commercially available 4-chloro-3-nitrobenzoic acid in dichloromethane (1 equiv) was added 4-dimethylaminopyridine (DMAP; 0.3 equiv) and *tert*-butanol (2 equiv). The *N*,*N*′-dicyclohexylcarbodiimide (DCC; 1 equiv) was added at 0 °C, and the mixture was stirred for 17 h at room temperature. The precipitate was filtered out under celite, and the organic layer was concentrated under vacuum. The residue was purified by flash-column chromatography on silica gel to provide the desired *tert*-butyl 4-chloro-3-nitrobenzoate intermediate (Fig. 3*A*).

General procedure B (ArS$_N$2 reaction) (5). To the *tert*-butyl 4-chloro-3-nitrobenzoate intermediate (1 equiv) in dry DMSO (5 mL) was added K_2CO_3 (2 equiv) and 1-adamantylamine (1.2 equiv). The mixture was stirred for 17 h at 60 °C. The solution was poured into water, and the organic layer was extracted three times with ethyl acetate. After drying with anhydrous magnesium sulfate, the solvents were removed under vacuum. The residue was purified by flash-column chromatography on silica gel to provide the desired *tert*-butyl 4-(adamanthyl-amino)-3-nitrobenzoate SRS16-79 (Fig. 3*A*).

General procedure C (hydrogenolysis). The *tert*-butyl 4-(adamanthyl-amino)-3-nitrobenzoates SRS16-79 (1 equiv) was dissolved in MeOH (10 mL) and hydrogenated (H_2 gas) over 10% $Pd(OH)_2$ on charcoal (0.1 equiv) for 17 h at room temperature. The solution was filtered through a pad of celite, and volatiles were removed under vacuum. The residue was purified by flash-column chromatography on silica gel to provide the desired *tert*-butyl 3-amino-4-(adamantylamino)benzoate SRS16-82 (Fig. 3*A*).

General procedure D (imine formation). To the *tert*-butyl 3-amino-4-(adamantylamino)benzoate SRS16-82 (1 equiv) in ethanol (4 mL) and drops of dry HCl 4.0 M in dioxane (10 μL) was added pyrimidine aldehyde (1.1 equiv). The mixture was stirred at 80 °C during 4 h. The solvent was evaporated. The residue was purified by flash-column chromatography on silica gel to provide the desired (*Z*)-*tert*-butyl 4-(adamantylamino)-3-(pyrimidin-5-ylmethyleneamino)benzoate SRS16-86 (Fig. 3*A*).

Spectroscopic Characterization.

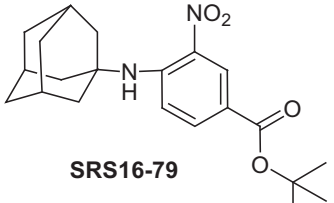

SRS16-79

After the above general procedures A and B, the reaction was purified by flash-column chromatography on silica gel to provide the desired *tert*-butyl 4-(adamantylamino)-3-nitrobenzoate (SRS16-79) (1.08 g, 2.903 mmol, 75%). ^{1}H NMR (400 MHz, $CDCl_3$) δ 8.80 (d, J = 2.1 Hz, 1H), 8.56 (s, 1H), 7.92 (dd, J = 9.2, 2.1 Hz, 1H), 7.19 (d, J = 9.2 Hz, 1H), 2.21 (s, 2H), 2.12 (s, 5H), 1.95 (s, 1H), 1.90 (s, 2H), 1.77 (s, 5H), 1.58 (s, 9H); liquid chromatography (LC)/MS (APCI+, *M+1*) 373.03.

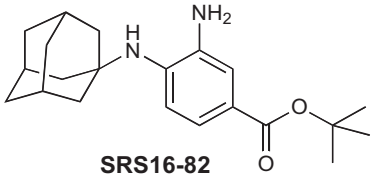

SRS16-82

After the above general procedure C, the crude reaction mixture was purified by column chromatography (dichloromethane:methanol = 40:1) to provide the desired *tert*-butyl 3-amino-4-(2-adamantylamino)-benzoate (SRS16-82) [700 mg, 2.046 mmol, 88% (3 steps)]. ^{1}H NMR (400 MHz, $CDCl_3$) δ 7.47 (dd, J = 8.4, 1.9 Hz, 1H), 7.38 (d, J = 1.8 Hz, 1H), 6.93 (d, J = 8.4 Hz, 1H), 3.33 (s, 2H), 2.15 (s, 3H), 1.99 (s, 6H), 1.72 (s, 6H), 1.57 (s, 9H); LC/MS (APCI+, *M+1*) 343.09.

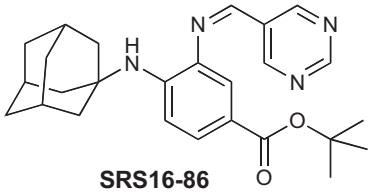

SRS16-86

After the above general procedure D, the reaction was purified by flash-column chromatography on silica gel to provide the desired *tert*-butyl 4-(adamantylamino)-3-(pyrimidin-5-ylmethyleneamino)benzoate (SRS16-86) (200 mg, 0.462 mmol, 89%). ^{1}H NMR (400 MHz, $CDCl_3$) δ 9.30 (s, 10H), 9.29–9.15 (m, 33H), 8.66 (d, J = 4.1 Hz, 14H), 7.99–7.70 (m, 28H), 7.19–6.92 (m, 14H), 5.58 (s, 13H), 2.13 (d, J = 46.0 Hz, 117H), 2.00 (s, 21H), 1.75 (s, 106H), 1.71–1.54 (m, 140H); low-resolution mass spectrometry (FAB+, *M*+) 432.1; HRMS (FAB+) calculated for C16H24N2O2: 432.2525; found: 432.2541.

Statistics. For all experiments, differences of datasets were considered statistically significant when P values were lower than 0.05, if not otherwise specified. Statistical comparisons were performed using the two-tailed Student t test. Asterisks are used in the figures to specify statistical significance ($^*P < 0.05$; $^{**}P < 0.02$; $^{***}P < 0.001$). P values in survival experiments (Kaplan–Meier plots) were calculated using GraphPad Prism Version 5.04 software. Statistics are indicated as SD (not to SEM).

1. Traykova-Brauch M, et al. (2008) An efficient and versatile system for acute and chronic modulation of renal tubular function in transgenic mice. *Nat Med* 14(9):979–984.
2. National Research Council (2011) *Guide for the Care and Use of Laboratory Animals* (National Academies Press, Washington, DC), 8th Ed.
3. Linkermann A, et al. (2012) Dichotomy between RIP1- and RIP3-mediated necroptosis in tumor necrosis factor-α-induced shock. *Mol Med* 18:577–586.
4. Mulay SR, et al. (2013) Calcium oxalate crystals induce renal inflammation by NLRP3-mediated IL-1β secretion. *J Clin Invest* 123(1):236–246.
5. Beaulieu PL, et al. (2006) Improved replicon cellular activity of non-nucleoside allosteric inhibitors of HCV NS5B polymerase: From benzimidazole to indole scaffolds. *Bioorg Med Chem Lett* 16(19):4987–4993.

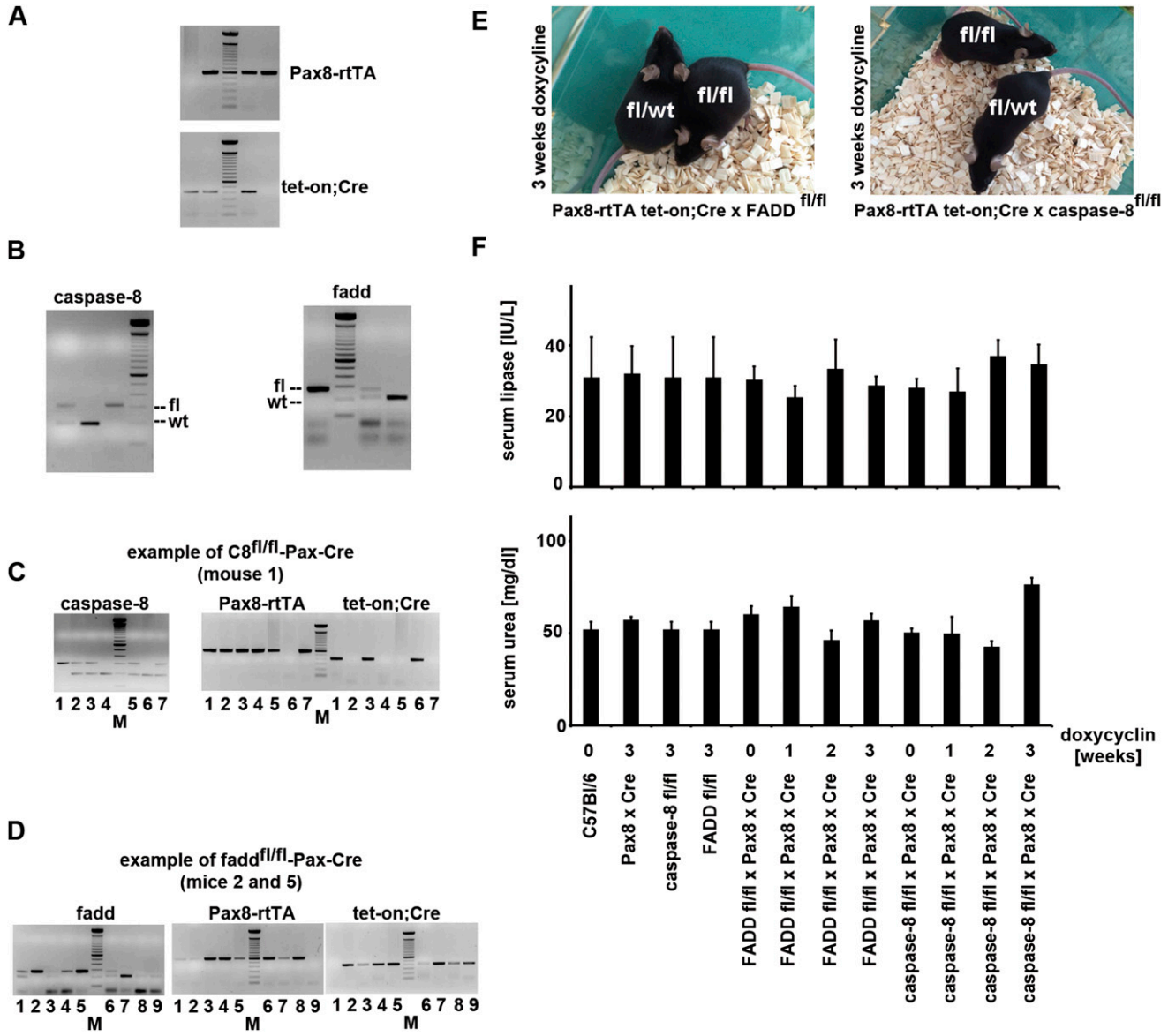

Fig. S1. Generation of doxycyclin-inducible kidney tubular specific conditional FADD- and caspase-8 knockout mice. (*A–D*) Representative genotyping of either FADD-inducible or caspase-8 doxycyclin-inducible kidney tubular-specific conditional knockout mice. (*E*) Indistinguishability of fl/wt and fl/fl mice after doxycyclin treatment for 3 wk via the drinking water (see *Materials and Methods* for details). (*F*) Mice of the indicated genotypes were treated for 0 wk, 1 wk, 2 wk, or 3 wk with doxycyclin before detection of serum lipase (*Upper*) and serum urea (*Lower*) levels (n = 3–8 per group for all blood values).

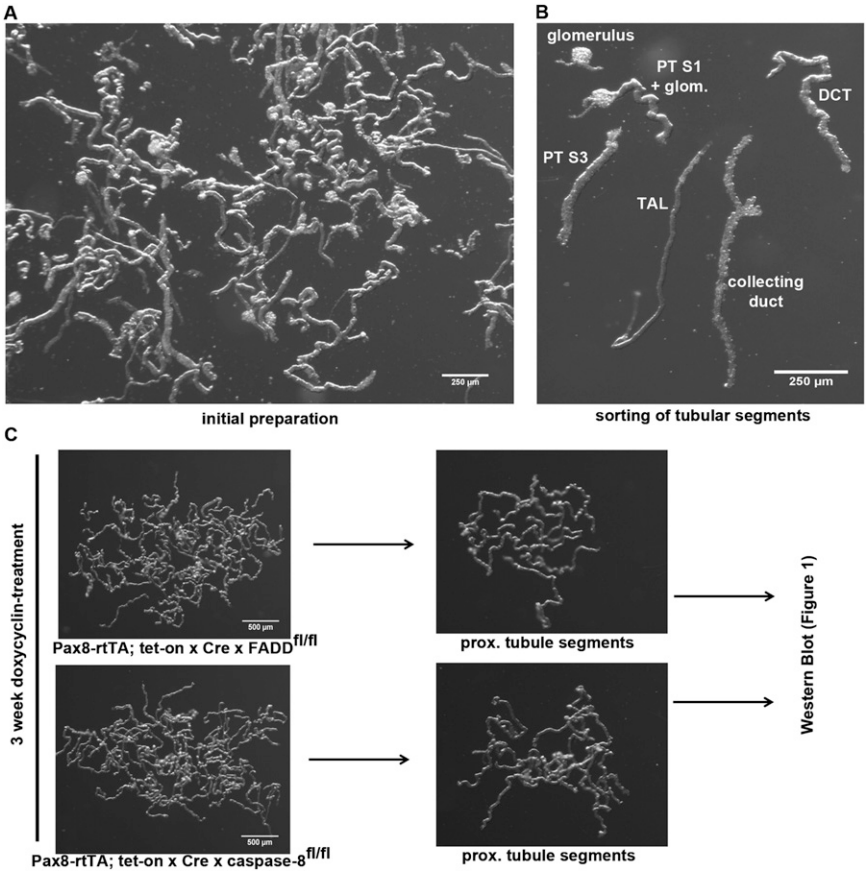

Fig. S2. Preparation of murine renal tubules for Western blot analysis and microperfusion movies. (*A*) Classical appearance after performance of the initial enzymatic preparation steps (see *Materials and Methods* for details). (*B*) Overview of hand-picked tubular segments. For Western blot analysis, proximal tubules were collected due to the very high susceptibility to undergo necrosis in acute kidney injury. (*C*) Doxycyclin-fed mice were killed after 3 wk of transactivator induction, and renal tubules were collected. Proximal tubular segments were subsequently pooled and loaded onto gels for Western blotting in Fig. 1. DCT, distal convoluted tubule; TAL, thick ascending limb.

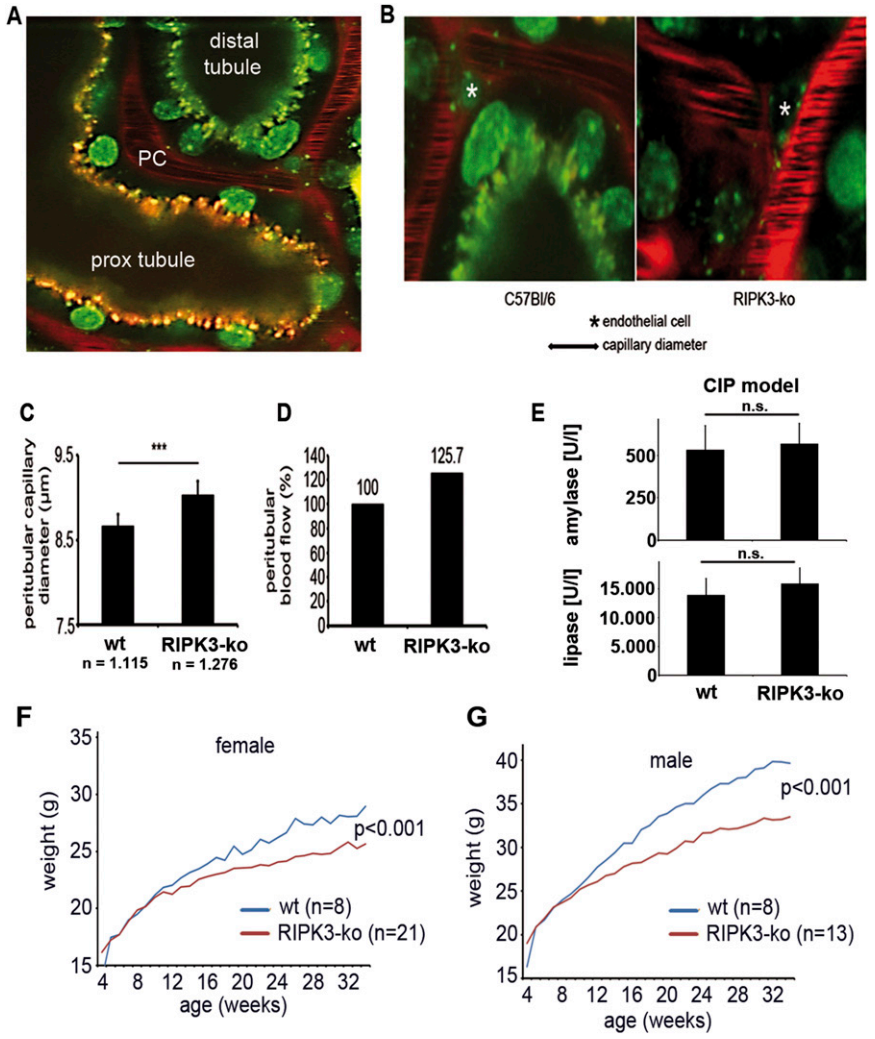

Fig. S3. RIPK3-deficient mice have a phenotype. (*A*) Example of high-resolution intravital microscopy. Green, autofluorescence of the kidney tubules; red, 70 kDa rhodamine dextran (applied via a jugular catheter); yellow, Texas Red (2 kDa) dye, which is freely filtered in the glomerular and reabsorbed in the proximal tubule, counterstaining the endolysosomal compartment; PC, peritubular capillary. For a dynamic impression on how this endolysosomal compartment works, compare Movie S2. (*B* and *C*) Intravital microscopy reveals significantly increased peritubular diameters in untreated RIPK3-deficient mice compared with WT littermates. Data in *C* were generated by counting the diameters of peritubular capillaries at a number of at least 1.115 per group. (*D*) Based on the data presented in *B*, the increase in peritubular diameters is associated with 125.7% overall organ perfusion in RIPK3-deficient mice. (*E*) Model of cerulein-induced pancreatitis (CIP) in WT and RIPK3-deficient mice. No significant protection from increased serum concentrations of serum lipase or serum amylase was detected in RIPK3-deficient mice compared with WT mice ($n = 7$ mice per group). (*F* and *G*) Failure to gain overall body weight in both female (*Left*) and male (*Right*) RIPK3-deficient mice compared with corresponding littermates, followed for 30 wk after an age of 4 wk ($n = 8$–21 per group).

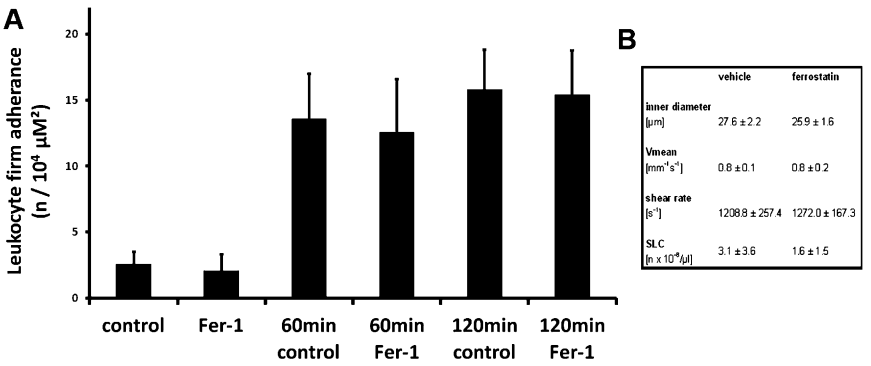

Fig. S4. Leukocyte adherence remains unchanged in IRI of the cremaster muscle upon addition of Fer-1. (*A*) Intravital evaluation of intravascular firm adhesion of leukocytes in postcapillary venules following 1 h and 2 h after onset of reperfusion. (*B*) Measurement of microhemodynamic parameters and systemic leukocyte counts, as indicated, based on intravital microscopy in the presence and absence of Fer-1.

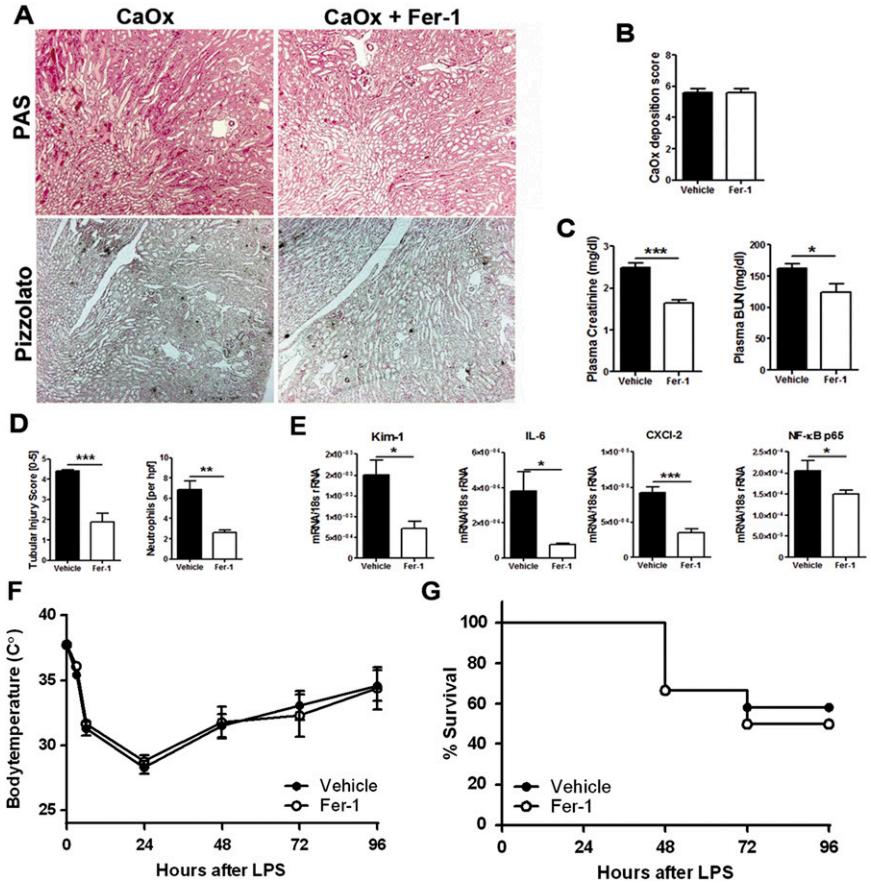

Fig. S5. Ferroptosis contributes to crystal-induced acute kidney injury, but not to the LPS-induced shock model. (*A*) PAS and Pizzolato staining of mice treated with CaOx and Fer-1. (*B*) CaOx deposition is not different between the two groups. (*C*) Evaluation of functional markers of acute kidney injury in mice that underwent CaOx-induced nephropathy. (*D*) Fer-1 significantly reduces the ultrastructural damage in CaOx nephropathy. (*E*) Significant reduction of expression of Kim-1 (TIM-1), IL-6, CXCL2, and p65 in the Fer-1–treated Ca-Ox model (*$P = 0.05$–0.02, **$P = 0.02$–0.001, ***$P \leq 0.001$; $n = 8$–10 per group). (*F* and *G*) In the model of LPS-induced septic shock, 12 mice per group were injected intraperitoneally with LPS as described in *SI Materials and Methods*. (*F*) Temperature drop and (*G*) overall survival rates following 96 h after LPS injection ($n = 12$ per group, error bars indicate SEM).

Table S1. Microsomal stability of SRS15-72A in mouse

Test compound	Elimination rate constant (*k*)	Half-life ($t_{1/2}$), min	Intrinsic clearance (CLint), mL/min per g liver
SRS15-72A	0.3419	2.0	35.90
Ethoxycoumarin	0.1591	4.4	16.71

Microsomal stability (mouse, compound concentration = 0.5 μM). Microsomal stability and intrinsic clearances of SRS15-72A in hepatic microsomes. Ethoxycoumarin was used as a control compound. Half life more than 90 min was reported as >90, and less than 1.4 was reported as <1.4. Rate constants for microsomes less than 0.0048 or negative were reported as <0.0048, and more than 0.48 were reported as >0.48.

Table S2. Microsomal stability of SRS15-72A in mouse

Test compound	Elimination rate constant (*k*)	Half-life ($t_{1/2}$), min	Intrinsic clearance (CLint), mL/min per g liver
SRS15-72A	0.0045	154.0	0.47
Ethoxycoumarin	0.1885	3.7	19.79

Microsomal stability (mouse, compound concentration = 0.5 μM). Microsomal stability and intrinsic clearances of SRS15-72A in hepatic microsomes. Ethoxycoumarin was used as a control compound. Half life more than 90 min was reported as >90, and less than 1.4 was reported as <1.4. Rate constants for microsomes less than 0.0048 or negative were reported as <0.0048, and more than 0.48 were reported as >0.48.

Table S3. Stability of SRS15-72A and SRS15-72B in mouse plasma (strain C57BL/4)

			Condition			
			Room temperature		Wet ice	
Compound name	Parent (*m/z*)	Time point, min	Peak area ratio	% remaining	Peak area ratio	% remaining
SRS15-72A	405	0	2.0737	100.0	2.6066	100.0
SRS15-72A	405	15	1.1581	55.8	2.0815	79.9
SRS15-72A	405	30	0.5320	25.7	1.6279	62.5
SRS15-72A	405	60	0.2502	12.1	1.4397	55.2
SRS15-72A	405	120	0.0841	4.1	1.2446	47.7
SRS15-72B	407	0	5.8556	100.0	6.9233	100.0
SRS15-72B	407	15	0.6709	11.5	5.7631	83.2
SRS15-72B	407	30	0.0885	1.5	4.7595	68.7
SRS15-72B	407	60	0.0206	0.4	3.4547	49.9
SRS15-72B	407	120	0.0159	0.3	1.9564	28.3

Percent remaining, percentage of peak area at each time point compared with peak area at 0 min.

Table S4. Stability of SRS16-80 and SRS16-86 in mouse plasma (strain C57BL/6)

Compound name	Parent (*m/z*)	Time point, min	Sum of peak	% remaining
SRS16-80	419.2	0	0.3820	100.0
SRS16-80	419.2	15	0.0911	23.8
SRS16-80	419.2	30	0.0379	9.9
SRS16-80	419.2	60	0.0170	4.5
SRS16-80	419.2	120	0.0095	2.5
SRS16-86	433.6	0	0.9018	100.0
SRS16-86	433.6	15	0.7414	82.2
SRS16-86	433.6	30	0.7800	86.5
SRS16-86	433.6	60	0.7568	83.9
SRS16-86	433.6	120	0.5758	63.9

Temperature, 37 °C. Percent remaining, percentage of peak area at each time point compared with peak area at 0 min.

Table S5. Microsomal stability of SRS16-80 and SRS16-86 in mouse

Test compound	Elimination rate constant (*k*)	Half-life ($t_{1/2}$), min	Intrinsic clearance (CLint), mL/min per g liver
SRS16-80	0.0089	77.7	0.94
SRS16-86	−0.0032	−213.7	−0.34
Ethoxycoumarin	0.2661	2.6	27.94

Microsomal stability (mouse, compound concentration = 0.5 μM). Microsomal stability and intrinsic clearances of SRS16-80 and SRS16-86 in hepatic microsomes. Ethoxycoumarin was used as a control compound. Half life more than 90 min was reported as >90, and less than 1.4 was reported as <1.4. Rate constants for microsomes less than 0.0048 or negative were reported as <0.0048, and more than 0.48 were reported as >0.48.

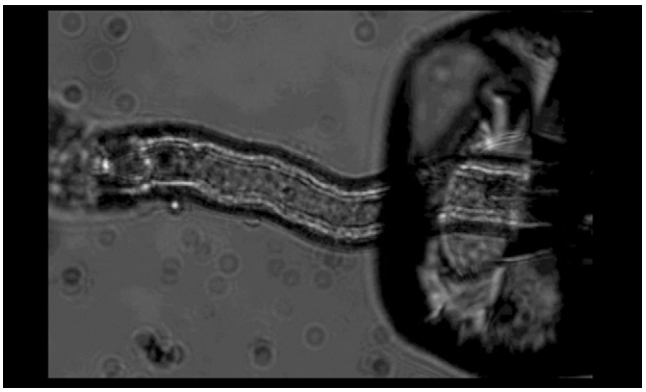

Movie S1. Synchronized tubular necrosis. Dynamics of synchronized tubular necrosis upon depletion of fatty acids (see *Materials and Methods* for details). Note that the synchronized event occurs secondarily after initial necrosis of individual cells. The overall appearance after the synchronized necrotic event morphologically very much resembles casts in urine sediments of patients with acute tubular necrosis (ATN), the classical diagnosis of acute kidney injury (AKI).

Movie S1

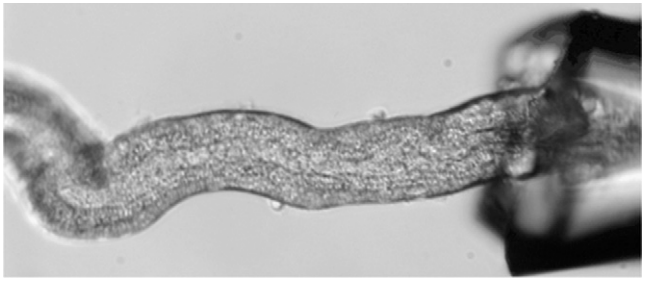

Movie S2. High-resolution movie and quality control of the functional endolysosomal compartment in freshly isolated renal proximal tubules. In the presence of fatty acids, synchronized necrosis does not spontaneously occur within the first hour of video monitoring. These preparations were used for all subsequent tubule experiments.

Movie S2

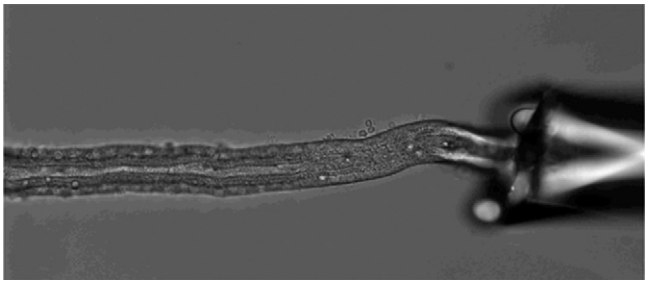

Movie S3. Erastin application induces synchronized tubular necrosis. In the presence of fatty acids, synchronized necrosis occurs within minutes [full movies range from 1 to 20 min (Movie S3) and 1–30 min (Movie S4 in higher resolution) after erastin addition to the perfusion solution]. Movies S3 and S4 represent two examples of this event in completely independent settings.

Movie S3

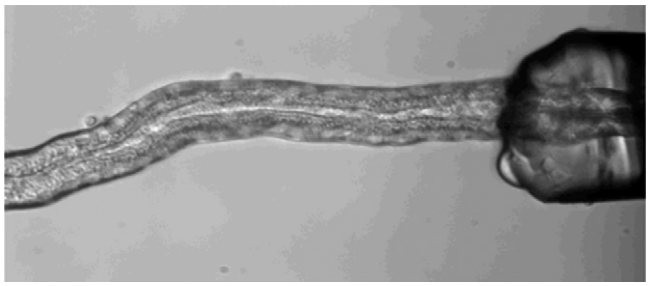

Movie S4. Erastin application induces synchronized tubular necrosis. In the presence of fatty acids, synchronized necrosis occurs within minutes [full movies range from 1 to 20 min (Movie S3) and 1–30 min (Movie S4 in higher resolution) after erastin addition to the perfusion solution]. Movies S3 and S4 represent two examples of this event in completely independent settings.

Movie S4